*Acta Oceanol. Sin.*, 2022, Vol. 41, No. 5, P. 51–63
https://doi.org/10.1007/s13131-021-1874-3
http://www.aosocean.com
E-mail: ocean2@hyxb.org.cn

# Short-term variations and influencing factors of suspended sediment concentrations at the Heisha Beach, Guangdong, China

Jintang Ou[1, 3], Haoyan Dong[2, 3], Liangwen Jia[1, 3, 4*], Xiangxin Luo[3, 4, 5*], Zixiao He[1, 3], Kanglin Chen[2, 3], Jing Liu[1, 3], Yitong Lin[1, 3], Mingdong Yu[2, 3], Mingen Liang[1, 3]

[1] School of Marine Engineering and Technology, Sun Yat-sen University, Guangzhou 510275, China

[2] School of Marine Sciences, Sun Yat-sen University, Guangzhou 510275, China

[3] Southern Marine Science and Engineering Guangdong Laboratory (Zhuhai), Zhuhai 519080, China

[4] Guangdong Provincial Engineering Research Center of Coasts, Islands and Reefs, Guangzhou 510275, China

[5] Institute of Estuarine and Coastal Research, School of Marine Engineering and Technology, Sun Yat-sen University, Guangzhou 510275, China

Received 7 May 2021; accepted 21 June 2021

**Abstract**

Knowledge of sediment variation processes is essential to understand the evolution mechanism of beach morphology changes. Thus, a field measurement was conducted at the Heisha Beach, located on the west coast of the Zhujiang River (Pearl River) Estuary, to investigate the short-term variation in suspended sediment concentrations (SSCs) and the relationship between the SSC and turbulent kinetic energy, bottom shear stress (BSS), and relative wave height. Based on extreme event analysis results, extreme events have a greater influence on turbulent kinetic energy than SSC. Although a portion of the turbulent kinetic energy dissipates directly into the water column, it plays an important role in suspended sediment motion. Most of the time, the wave-current interaction is strong enough to drive sediment incipience and resuspension. When combined, the wave-current interaction and wave-induced BSSs have a greater influence on suspended sediment transport and SSC variation than current-induced BSS alone. The relative wave height also has a strong correlation with SSC, indicating that the combined effect of water depth and wave height significantly impacts SSC variation. Water depth is mainly controlled by the tide on the beaches; thus, the effects of tides and waves should be conjunctively considered when analyzing the factors influencing SSC.

**Key words:** Heisha Beach, suspended sediment concentration variation, turbulent kinetic energy, bottom shear stress, relative wave height

**Citation:** Ou Jintang, Dong Haoyan, Jia Liangwen, Luo Xiangxin, He Zixiao, Chen Kanglin, Liu Jing, Lin Yitong, Yu Mingdong, Liang Mingen. 2022. Short-term variations and influencing factors of suspended sediment concentrations at the Heisha Beach, Guangdong, China. Acta Oceanologica Sinica, 41(5): 51–63, doi: 10.1007/s13131-021-1874-3

## 1 Introduction

Nearshore environments provide important habitats for coastal and marine life and support many human activities, including natural resource development and transportation. Knowledge of the physical and biogeochemical processes in these coastal environments is essential for their management, and for promoting sustainable development for these regions (Bolaños et al., 2012).

One of the most important processes in the nearshore environment is sediment transport, which affects the water quality, turbidity, biogeochemistry, and morphology evolution, especially for sandy beaches (Bolaños et al., 2012). The sediment transport process controls the morphodynamic state of the beach, and the cross-shore and alongshore sediment transport gradients are the main drivers of beach morphology changes, forming different beach states including dissipative, reflective, and intermediate beaches. Additionally, the different beach profile shapes and ensuing wave transformation patterns create different spatial sediment transport patterns (Aagaard et al., 2013). Thus, knowledge of sediment variation processes is essential to understand the evolution mechanism of beach morphology changes.

The sediment movement process on the beaches mainly depends on the hydrodynamic conditions and the corresponding suspended sediment concentrations (SSCs) (Pang et al., 2019). In the nearshore area, the hydrodynamic conditions control and affect sediment resuspension, mixing, and transport processes (Jing and Ridd, 1996); therefore, the roles of the different hydrodynamic factors on SSC need to be examined on different time scales.

Turbulent motion is one of the most critical contributors for sediment suspension and increasing SSCs (Aagaard and Hughes,

---

Foundation item: The National Key Research and Development Program of China under contract No. 2016YFC0402603; the Guangdong Provincial Department of Natural Resources Project under contract No. 42090038; the Guangdong Provincial Department of Ocean and Fisheries Project under contract No. 42090033.

*Corresponding author, E-mail: jialwen@126.com; luoxx6@mail.sysu.edu.cn

2006) by enhancing the current-induced bed shear stress (LeClaire and Ting, 2017), as has been confirmed by field observations and sediment transport models (Pang et al., 2020). A linear relationship was found between the net sediment flux and the net turbulent kinetic energy (TKE) flux over one wave cycle. Net onshore sediment transport is always associated with net positive (onshore) TKE flux (LeClaire and Ting, 2017). SSC in the water column under the waves depends on the balance between upward- and downward-directed sediment fluxes. In most sediment concentration models, upward fluxes depend on gradient diffusion and sediment pick-up (Nielsen, 1992). Gradient diffusion can be caused by small-scale turbulence due to friction between the (orbital) fluid motion and the (flat) seabed, whereas sediment pick-up can be caused by the lifting of coherent packages of sand by turbulent vortices produced by the interaction of fluid with bedforms, such as wave ripples (Aagaard and Hughes, 2010). Field observations and sediment transport models have confirmed that increased TKE intensity increases the SSC in the water (Hansen and Svendsen, 1984; Yoon and Cox, 2012). Therefore, to investigate the SSC variation mechanism on the beaches thoroughly, it is important to examine the influence of turbulent motion.

By utilizing fast response instruments to monitor the amount of sediment in suspension (Brenninkmeyer, 1976), researchers have observed short periods of high SSC and TKE when sediments reach high levels (1 m) in the water column (Jaffe and Sallenger, 1992). These intense periods, called extreme events in this study, are separated by longer quiescent periods with a smaller magnitude of SSCs, and the suspension is confined near the bed. Field studies have confirmed that extreme events control sediment suspension in the surf zone. It was demonstrated that “large” suspension events, which exceeded the mean plus three standard deviations of the time series, accounted for 10% of the total record fraction, but these events contained approximately 15%–35% of the SSC and drove the onshore sediment transport (Jaffe and Sallenger, 1992). Furthermore, intermittent TKE events in plunging breakers, which accounted for 7% of the records, could contain 40% of the TKE for the coherent event (Cox and Anderson, 2001). The importance of intermittent suspension to sediment transport has been demonstrated by showing the significance of the coupled fluctuations of velocity and SSC in the sediment flux calculation (Ogston and Sternberg, 1995; Yoon and Cox, 2012). It was shown that the correlated TKE events (the simultaneous occurrence of extreme SSC and TKE events) accounted for 12.2% of the total TKE time records, and 38.1% of the total turbulent motions were associated with 42.9% and 40.0% of the SSC events and total sediment concentrations, respectively (Pang et al., 2020). Therefore, to elucidate the sediment suspension and transport processes, identifying the intermittent features of SSC and TKE is vital.

Bottom shear siress (BSS) also plays an important role in sediment mobilization and the resulting suspended sediment transport. Shear stress that exceeds a threshold indicates sediment entrainment and can result in beach morphology evolution (Maity and Maiti, 2016). Increased SSC usually corresponds with a large combined wave-current BSS. In shallow coastal waters, both wave and current movements are important for sediment transport and can enhance bed turbulence and increase BSS (Jing and Ridd, 1996). It has been shown (Grant and Madsen, 1979) that shear stresses are altered when waves and currents coexist in a region because the turbulence generated by the wave-current interaction (WCI) near the bed differs from the stresses that occur from only waves or currents. Thus, evaluating the effect of WCI on BSS calculations is necessary to analyze the relationship between BSS and SSC accurately.

Moreover, the importance of relative wave height to sediment suspension and the subsequent SSCs on the beaches also need to be further studied. Relative wave height ($H_r$) is the ratio of wave height to water depth ($h$), and the tide mainly controls $h$ in the nearshore regions. Generally, wave height variations are the primary cause of variations in the average SSC in the water column due to their significant contribution to the sediment suspension mechanism compared to other factors, such as bed configuration and mean current (Aagaard and Greenwood, 1995; Liang et al., 2007; Pang et al., 2020). In the coastal zone, sand transport is strongly dependent on $H_r$, particularly under small velocity conditions (0.1–0.6 m/s) (Van Rijn, 2007). These findings indicate that $H_r$ significantly affects suspended sediment transport on the beaches.

It has been proven that turbulence motion, BSS and $H_r$ significantly influence sediment suspension on the beaches. In this paper, the effect of TKE, BSS, and $H_r$ on SSC variation have been studied by evaluating the relationship between the intermittent extreme events of TKE and SSC, analyzing the contribution of BSS under the influence of WCI and examining the relative importance of tides and waves on SSC.

## 2 Study area

Field observations were conducted at the Heisha Beach (Guangdong, China), located on the west coast of the Zhujiang River (Pearl River) Estuary, and the observation instrument was installed on the foreshore east of Heisha Beach (Fig. 1b). The Heisha Beach is composed of black sand with a gentle slope, and is located adjacent to the Huangmaohai Estuary in the east and the Taishan Nuclear Power Plant in the west (Fig. 1a). The surrounding islands include Dajin and Hebao Islands at the mouth of the Huangmaohai Estuary and Shangchuan and Xiachuan Islands to the west. From 1993 to 2001, approximately half of the beaches to the west of Heisha Beach were reclaimed to construct the Taishan Nuclear Power Plant.

According to data obtained from the Shangchuan Island tide gauge station, irregular semidiurnal tides prevail at the Heisha Beach, with a mean tidal range of 1.5–2.0 m.

The wave conditions in the dry and flood seasons were determined based on the 1982 measured wave data from the Hebao Island hydrological station. During the dry season, the highest 10% of the wave height ranges from 0.27–2.40 m with a mean value of approximately 1.26 m, and the wave period ranges from 3.4–7.8 s with a mean value of 5.6 s. During the flood season, the highest 10% of the wave height ranges from 0.48–2.81 m with a mean value of approximately 1.08 m, and the wave period ranges from 2.9–7.8 s with a mean value of 5.1 s. The wave directions are mainly southeast in the dry season, and in the flood season, they are primarily south and southeast, and sometimes east and southwest.

## 3 Methodology

### 3.1 *Instrument deployment*

Field observations were conducted from August 9–12, 2019, at the foreshore of Heisha Beach. The observation interval (hereafter called “burst”) was 10 min, and 332 bursts with valid data were obtained.

An aluminum frame was equipped with a 6 MHz Nortek acoustic Doppler velocimeter (ADV) and an optical backscatter sensor (RBR-Tu.Iwave), and a 1 MHz Nortek acoustic wave and

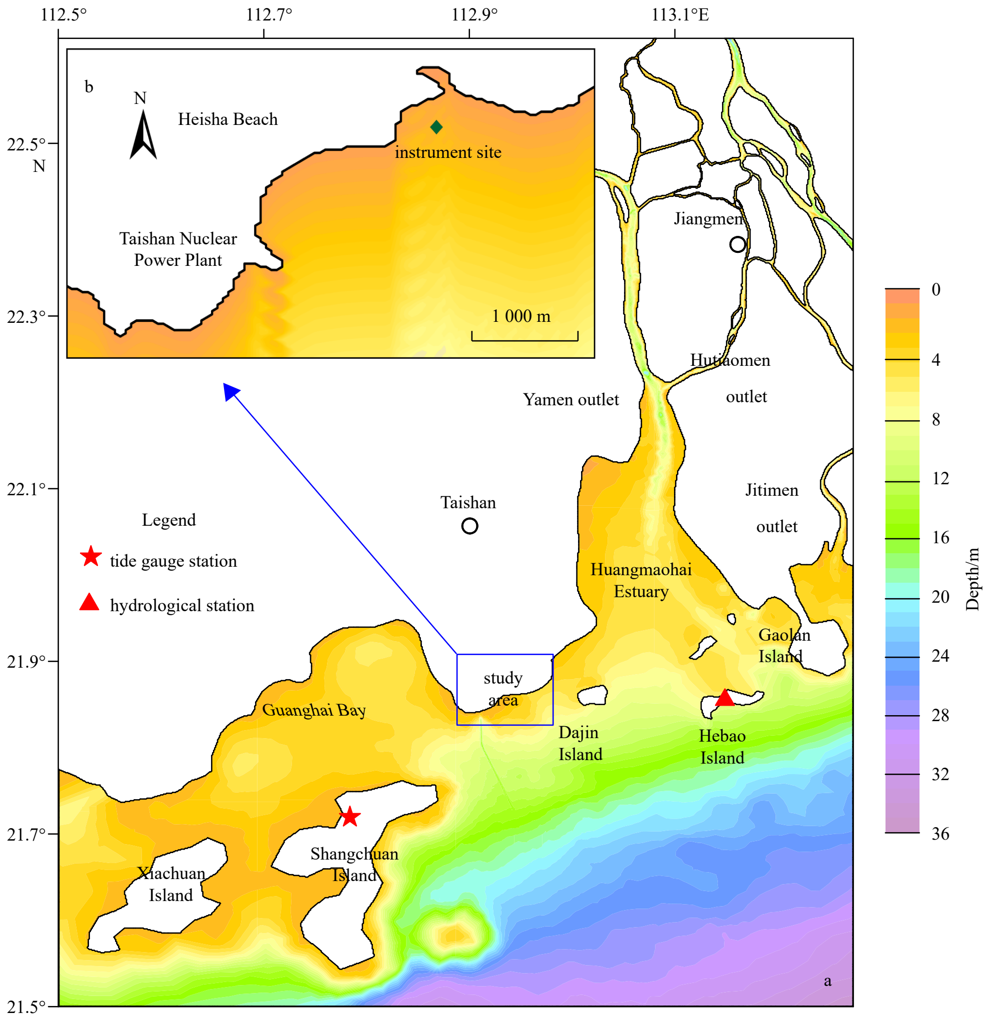

**Fig. 1.** Location of the study area (a) and instrument site (b).

current profiler (AWAC) was installed on a second frame. The ADV was used to record high-resolution 3D flow velocities in three directions: alongshore ($u$), cross-shore ($v$), and vertical ($w$). The ADV sensors faced downward and were located approximately 23 cm above the seabed. The velocity measurements were recorded every 10 min at 32 Hz for 5 min. The RBR-Tu.Iwave was utilized to measure turbidity and water depth ($h$). During Periods D1 and D2, the RBR-Tu.Iwave probe was located approximately 59 cm above the seabed, and measurements were performed at 0.2 Hz. During Period D3, the probe was located approximately 38 cm above the seabed, and measurements were performed at 6 Hz. The relationship between turbidity and SSC was calculated utilizing the linear least-squares fitting method, and the linear fitting value ($R^2$) was 0.99 (Fig. 2). The AWAC, with its probe located approximately 50 cm above the seabed, was used to record the mean wave height ($H_{\mathrm{m0}}$) and mean wave period ($T_{\mathrm{m0}}$). Therefore, the study data included 332 segments of 10 min synchronous measurement data, including high-resolution 3D flow velocity, water turbidity, $h$, $H_{\mathrm{m0}}$, and $T_{\mathrm{m0}}$.

### 3.2 *Methods*

#### 3.2.1 *TKE calculation*

Based on the data measured by ADV, the velocity direction is utilized to obtain the alongshore ($u$), cross-shore ($v$), and vertical ($w$) velocities. The TKE calculation equation utilized is as follows:

$$\mathrm{TKE} = \frac{1}{2}\rho(u'^2 + v'^2 + w'^2), \tag{1}$$

where $u'$, $v'$, and $w'$ are the turbulent oscillation components of the three directions, and $\rho$ is seawater density (1 025 kg/m³).

The frequency cut-off method is utilized to estimate the turbulent oscillation components. The cut-off frequency is determined by the slope break of the power spectral density curve of the velocity in each direction (Foster et al., 2006; Ruessink, 2010; Smyth and Hay, 2003). For example, the power spectrum in Fig. 3

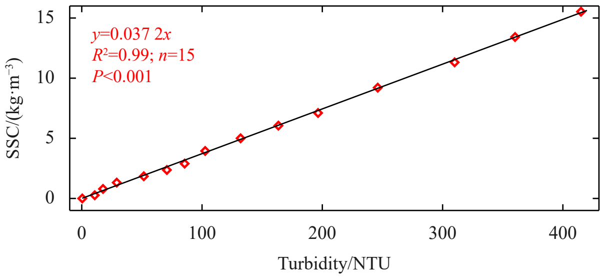

**Fig. 2.** Linear least-squares line of best fit between turbidity and SSC of the water samples.

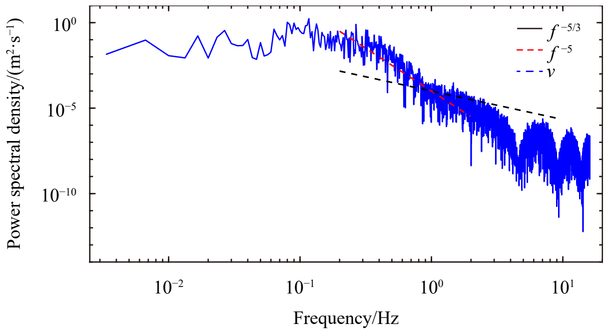

**Fig. 3.** Power spectral density of cross-shore velocity ($v$) vs. frequency (blue line) for Burst 19. The red and black dashed lines indicate different spectral slopes.

shows a slope break at approximately 1 Hz, which indicates a change in the dominance of wave and turbulent motion. This method has frequently been utilized in previous studies with different cut-off frequencies (Foster et al., 2000; Kos'yan et al., 1996; Smyth and Hay, 2003).

### 3.2.2 *BSS calculation*

The effect of the WCI on BSS was calculated based on the theory of Grant and Madsen (1979) , in which an enhanced drag exists at the outer edge of the wave-current boundary layer. This drag is a function of the near-bottom wave orbital velocity ($U_w$), mean current ($U_c$), wave frequency ($\omega$), bottom roughness height ($z_0$), and the angle between the wave propagation direction and the current ($\varphi_c$). The wave-current boundary layer thickness, called reference height ($\delta_{cw}$) in this study, is estimated as 5% of the mean $h$ (Jia et al., 2014) , which was 1.52 m during the observation period; therefore, $\delta_{cw}$ was approximately 0.08 m.

The maximum BSS ($\tau_{b,\,max}$) for the wave-current combination is calculated as follows:

$$\tau_{b,\,max} = \tau_w + \tau_c, \tag{2}$$

where $\tau_c$ and $\tau_w$ are the current- and wave-induced BSS, respectively. $\tau_w$ is calculated as follows:

$$\tau_w = \rho u_{*w}^2 = \frac{1}{2}\rho f_w U_w^2, \tag{3}$$

where $u_{*w} = \sqrt{\frac{1}{2}f_w}U_w$ is the wave-induced shear friction velocity. Based on the linear wave theory, $U_w$ can be computed as follows:

$$U_w = \frac{\pi H_{m0}}{T_{m0}\sinh(2\pi h/L)}, \tag{4}$$

where $H_{m0}$ is the mean wave height, $T_{m0}$ is the mean wave period, $h$ is the water depth and $L$ is the wave length. $L$ can be calculated by iterative computations through the linear wave dispersion relation:

$$L = \frac{gT_{m0}^2}{2\pi}\tanh\left(\frac{2\pi h}{L}\right). \tag{5}$$

The wave friction factor ($f_w$) can be calculated via Eq. (6) (Jonsson, 1966) and Eq. (7) (Swart, 1974):

$$f_w = \exp\left[-6 + 5.2\left(\frac{A_\delta}{k_s}\right)^{-0.19}\right], \tag{6}$$

$$f_w = 0.002\,51\exp\left[5.21\left(\frac{A_\delta}{k_s}\right)^{-0.19}\right],\quad A_\delta/k_s \leqslant 1.57, \tag{7}$$

where $A_\delta = U_w T/(2\pi)$ is the near bottom excursion amplitude, $T$ is the wave period, and $k_s$ is the bottom physical roughness, which is usually utilized to determine the $z_0$ ($z_0 = k_s/30$ in the turbulent conditions). $k_s$ is composed of three physical roughness measurements: (1) the particle roughness $k_{sg} = 2.5D$; (2) the bed form roughness $k_{sd} = 27.7H^2/\lambda$, where $H$ and $\lambda$ are the height and the length of sand wave respectively; (3) the bed load roughness, $k_{sc} = 1.142\,4D\frac{\tau_{sf}}{\tau_c + 0.2\tau_{sf}}$, $\tau_{sf} > \tau_{cr}$, in which $\tau_{cr}$ is the critical stress of sediment movement (as shown in Eq. (16)).

An initial current friction factor ($f_c$) that does not consider the wave effect is calculated as follows:

$$f_c = 2\left[\frac{\kappa}{\ln(30\delta_{cw}/k_s)}\right]^2, \tag{8}$$

where $\kappa$, the von Karman's constant, is 0.4.

The current-induced BSS and current-induced shear friction are calculated using Eqs (9) and (10), respectively, as follows:

$$\tau_c = \rho u_{*c}^2 = \frac{1}{2}\rho f_c u_c^2, \tag{9}$$

$$u_{*c} = \sqrt{\frac{1}{2}f_c}u_c, \tag{10}$$

where $u_c$ is the current at $\delta_{cw}$. The combined wave-current friction velocities are computed as follows:

$$u_{*cw} = (u_{*c}^2 + u_{*w}^2 + 2u_{*c}u_{*w}\cos\varphi_c)^{1/2}. \tag{11}$$

The apparent bottom roughness ($k_b$) , which indicates the turbulence level due to the wave-current boundary layer and physical bottom roughness, are calculated as follows (Signell et al., 1990):

$$k_b = k_s\left[24\frac{u_{*cw}}{U_w}\frac{A_\delta}{k_s}\right]^\beta, \tag{12}$$

where

$$\beta = 1 - \frac{u_{*c}}{u_{*cw}}. \tag{13}$$

The resultant $k_b$ is utilized in Eq. (8) as $k_s$ to calculate the combined wave-current friction factor ($f_{cw}$) for the next time step as follows:

$$f_{cw} = 2\left[\frac{\kappa}{\ln(30\delta_{cw}/k_b)}\right]^2. \tag{14}$$

To obtain a stable $f_{cw}$ value, iterations of this process are performed, in which $f_{cw}$ is substituted for $f_c$ in Eq. (10). Then, iterations of Eqs (10)–(14) are performed until the difference between the computed results of the last and next to last time step is less than the preset threshold ($10^{-6}$ in this study). Once the final $f_{\rm cw}$ has been obtained, the current shear stress, $\tau_{\rm c}=\frac{1}{2}\rho f_{\rm cw}u_{\rm c}^2$, is calculated in the presence of the wave.

The $\tau_{\rm b,max}$ for the wave-current combination, which does not consider the effect of the wave and current propagation directions on the combined wave-current BSS, is calculated via Eq. (2). In this study, the nonlinear combined wave-current BSS proposed by Soulsby et al. (1993) is utilized, which is calculated as follows:

$$\left\{\begin{aligned}\tau_{\rm cw}&=\left[\left(\tau_{\rm m}+\tau_{\rm w}\left|\cos\varphi_{\rm c}\right|\right)^2+\left(\tau_{\rm w}\sin\varphi_{\rm c}\right)^2\right]^{0.5},\\ \tau_{\rm m}&=\tau_{\rm c}\left[1+1.2\left(\frac{\tau_{\rm w}}{\tau_{\rm w}+\tau_{\rm c}}\right)^{3.2}\right],\end{aligned}\right. \tag{15}$$

where $\tau_{\rm m}$ is the mean BSS in the current direction and $\tau_{\rm cw}$ is the maximum BSS within a wave period; thereby, the effects of the wave and current propagation directions are considered in Eq. (15).

Additionally, the critical BSS ($\tau_{\rm cr}$) for sediment motion initiation is obtained via the following equation (Soulsby, 1997):

$$\tau_{\rm cr}=\theta_{\rm cr}(\rho_{\rm s}-\rho)gD_{50}, \tag{16}$$

where $\rho_{\rm s}$ are the density of quartz grain (2 650 kg/m$^3$), $D_{50}$ is the median grain size, and $\theta_{\rm cr}$ is the critical Shield's parameter for sediment motion initiation. $\theta_{\rm cr}$ is calculated via the following equation (Soulsby, 1997):

$$\theta_{\rm cr}=\frac{0.24}{D_*}+0.055[1-\exp(-0.02D_*)], \tag{17}$$

where $D_*$ is the dimensionless grain diameter given as

$$D_*=\left[\frac{g(s-1)}{\nu^2}\right]^{1/3}D_{50}, \tag{18}$$

where $s$ is the ratio of the quartz grain and seawater densities (2.59) utilized in Eq. (16) and $\nu$ is the kinematic viscosity of seawater (~$1.0\times10^{-6}$ m$^2$/s).

### 3.2.3 *Extreme event analysis*

In this study, the extreme event is defined as the signals exceed the 75th percentile of the overall data for single variable (Pang et al., 2020). Other studies have defined an extreme event as signals exceeding the mean value (Jaffe and Sallenger, 1992) or the mean value plus one standard deviation (Cox and Kobayashi, 2000). In this study, $n$ is the total number of data points, $m$ is the mean value of the data points, $n_1$ is the number of extreme event data points, and $m_1$ is the mean value of the extreme event data points. If an extreme event occurs simultaneously for two variables, this is defined as a correlated extreme event, where $n_0$ and $m_0$ are the number and mean value of correlated extreme event data points, respectively. Therefore, $n_1/n$ is the fraction of extreme events to total data points, $n_0/n$ is the fraction of correlated extreme events to total data points, and $n_1m_1/nm$ and $n_0m_0/nm$ represent the influence of extreme events of a single variable and correlated extreme events to the total record, respectively. The correlation between the two variables can be evaluated via an extreme event analysis, which is applicable for high-resolution data; therefore, this analysis method was utilized in this study to analyze the correlation between SSC and TKE, BSS, $h$, $H_{\rm m0}$, and $H_{\rm r}$.

### 3.2.4 *Pearson correlation coefficient and Spearman rank correlation coefficient*

The Pearson correlation coefficient ($r_{\rm p}$) is calculated as follows (Nahler, 2009):

$$r_{\rm p}=\frac{\sum\limits_{i=1}^{n}(y_i-\bar{y})(x_i-\bar{x})}{\left[\sum\limits_{i=1}^{n}(y_i-\bar{y})^2\sum\limits_{i=1}^{n}(x_i-\bar{x})^2\right]^{1/2}}=\frac{\sum\limits_{i=1}^{n}(y_i-\bar{y})(x_i-\bar{x})}{n\sigma_x\sigma_y}, \tag{19}$$

where $r_{\rm p}$ is the Pearson correlation coefficient of two variables ($x$ and $y$), $n$ is the number of data points, and $\sigma_x$ and $\sigma_y$ are the standard deviation of $x$ and $y$, respectively.

Spearman rank correlation (Spearman, 1904) is one of the oldest and best known of nonparametric functions. The Spearman rank correlation coefficient ($r_{\rm s}$) is generally expressed as follows (Zar, 1972):

$$r_{\rm s}=1-\frac{6\sum\limits_{i=1}^{n}d_i^2}{n(n^2-1)}, \tag{20}$$

where $n$ is the number of measurements for the two correlated variables ($x$ and $y$) and $d_i=\text{rank}\,(x_i)-\text{rank}\,(y_i)$ is the ranked difference between the $i$-th measurement for the two variables ($x$ and $y$).

The $r_{\rm p}$ is utilized to evaluate the linear correlation between the two variables that are normally or nearly unimodally distributed, and $r_{\rm s}$ is utilized to evaluate the monotonic correlation between the two variables that do not have repeated rank levels in the data point set. Compared with $r_{\rm p}$, $r_{\rm s}$ can be applied to more situations and with fewer data quality limitations.

### 3.2.5 *Surficial sediment particle size measurement*

During the observation period, 12 surficial sediment samples (HSW01–HSW12) were collected at the sampling site (Fig. 4). A Mastersizer 3000 laser analyzer was used to measure the sediment grain size distribution of the samples, and electron microprobe analysis was performed to examine the composition of the sediment. According to the measured results, the Heisha Beach

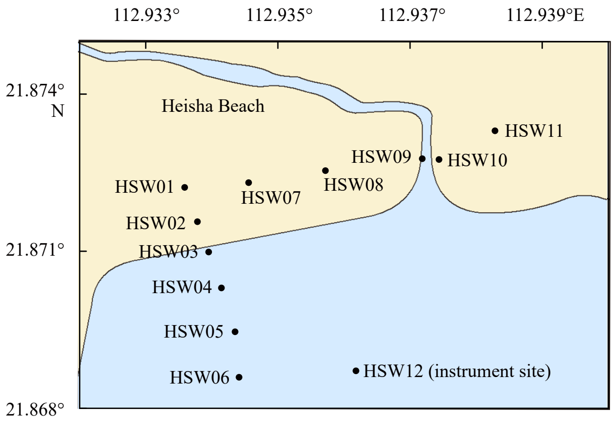

**Fig. 4.** Surficial sediment sampling locations.

sediment is primarily composed of sand, with smaller amounts of gravel and silt. The proportion of fine and very fine sand is relatively high, reaching 90% in the foreshore, while medium and coarse sand accounts for approximately 10% (except HSW07).

The mean grain size ($D_{\mathrm{me}}$), sorting coefficient (Sc), skewness (Sk) and kurtosis (Ku) are shown in Table 1, which are computed as follows (Folk and Ward, 1957):

$$D_{\mathrm{me}}=\frac{d_{16}+d_{50}+d_{84}}{3}, \tag{21}$$

$$\mathrm{Sc}=\frac{d_{84}-d_{16}}{4}+\frac{d_{95}-d_{5}}{6.6}, \tag{22}$$

$$\mathrm{Sk}=\frac{d_{84}+d_{16}-2d_{50}}{2(d_{84}-d_{16})}+\frac{d_{95}+d_{5}-2d_{50}}{2(d_{95}-d_{5})}, \tag{23}$$

$$\mathrm{Ku}=\frac{d_{95}-d_{5}}{2.44(d_{75}-d_{25})}, \tag{24}$$

where $d_j$ represents the corresponding grain size values at $j$% of the cumulative frequency curve.

The median grain size ($D_{50}$) range of the surficial sediment is 2.08ϕ–2.88ϕ, and at the instrument site (HSW12), $D_{50}$ is approximately 2.83ϕ (Table 1). The sorting degree in the offshore area is better than that of the area close to the backshore. Generally, Heisha Beach sediment can be characterized as negative skewness and moderate kurtosis, and the main components of the sediment, determined via electron microprobe analysis, are quartz and glauconite, which account for about 50% and 40% in the component distribution respectively (Fig. 5).

**Table 1.** Sediment parameters of the samples

| Sampling point | $D_{\mathrm{me}}$(ϕ) | $D_{50}$(ϕ) | Sc | Sk | Ku |
|---|---|---|---|---|---|
| HSW01 | 2.40 | 2.48 | 0.84 | −0.22 | 1.19 |
| HSW02 | 2.65 | 2.65 | 0.67 | −0.11 | 1.11 |
| HSW03 | 2.70 | 2.68 | 0.76 | −0.17 | 1.32 |
| HSW04 | 2.62 | 2.64 | 0.78 | −0.22 | 1.24 |
| HSW05 | 2.62 | 2.64 | 0.72 | −0.17 | 1.17 |
| HSW06 | 2.74 | 2.73 | 0.63 | −0.11 | 1.06 |
| HSW07 | 1.82 | 2.08 | 1.14 | −0.21 | 0.81 |
| HSW08 | 2.59 | 2.61 | 0.58 | −0.06 | 0.99 |
| HSW09 | 2.73 | 2.61 | 1.15 | 0.27 | 1.99 |
| HSW10 | 2.95 | 2.82 | 1.03 | 0.36 | 2.47 |
| HSW11 | 2.90 | 2.88 | 0.47 | 0.02 | 0.95 |
| HSW12 | 2.86 | 2.83 | 0.49 | −0.02 | 0.95 |

## 4 Results

### 4.1 *Characteristics of the hydrodynamic conditions*

Based on the tide data from the Shangchuan Island tide gauge station, all 332 bursts were divided into three periods: (1) Bursts 1–109 (Period D1) lasted from 16:10 on August 9 to 10:10 on August 10, (2) Bursts 110–213 (Period D2) lasted from 16:00 on August 10 to 9:10 on August 11, and (3) Bursts 214–332 (Period D3) lasted from 16:50 on August 11 to 12:30 on August 12. Each period contained a whole tidal cycle and lasted for about one day with continuous data gathering. Moreover, the tidal ranges of three periods (1.42 m, 1.70 m, and 1.95 m respectively) were apparently different (Fig. 6a), which indicated that the tide impacts of three periods were also different.

According to the data measured at the instrument site (Fig. 1b) during the observation period, except for the extremely low water period, $h$ ranged from 0.75–2.14 m during the observation period (Fig. 6b). The $H_{\mathrm{m0}}$ ranged from 0.24–1.14 m, and the maximum wave height occurred in Period D3. During Periods D2 and D3, the variation trends of $h$ and $H_{\mathrm{m0}}$ were similar (Fig. 6c). $T_{\mathrm{m0}}$ ranged from 1.06–3.38 s and the $T_{\mathrm{m0}}$ values were generally less than 2 s in Period D1, while in Periods D2 and D3, they were generally greater than 2 s (Fig. 6d).

The variation in the mean current velocity of the bursts is presented in Figs 6e and f. Generally, $u$ was slightly greater than $v$ with ranges of −0.11 m/s to 0.35 m/s, and −0.23 m/s to 0.07 m/s, respectively. The current flowed offshore most of the time, and offshore velocity was greater than onshore velocity (Fig. 6e). During Period D1, $u$ generally ranged from −0.1 m/s to 0.1 m/s, and during Periods D2 and D3, $u$ typically exceeded 0.1 m/s (Fig. 6f).

### 4.2 *The variation of SSCs*

As shown in Fig. 7, during the observation period, the SSC ranged from 0.70–9.55 kg/m$^3$. Generally, the SSC increased from Period D1 to D3 and was significantly higher in Periods D2 and D3 compared to Period D1. The SSC decreased between Bursts 1–100 and increased between Bursts 101–264 with mean values of 1.40 kg/m$^3$ and 4.78 kg/m$^3$, respectively. The SSCs from Bursts 235–264 were significantly higher than the other bursts, with a mean value of 7.93 kg/m$^3$, and the SSC decreased slowly from Bursts 265–332, with a mean value of 6.24 kg/m$^3$, which is higher than the mean value of Bursts 1–100.

The extreme SSC events were analyzed in this study, and the

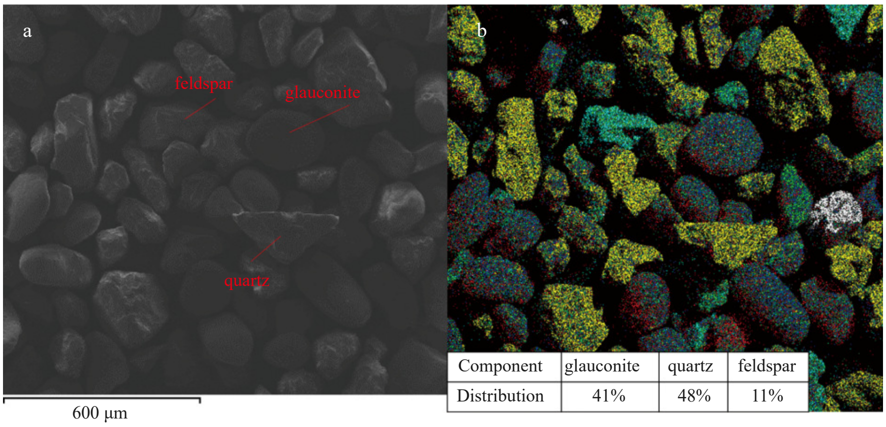

| Component | glauconite | quartz | feldspar |
|---|---|---|---|
| Distribution | 41% | 48% | 11% |

**Fig. 5.** Electron microscope image (a) and component distribution (b).

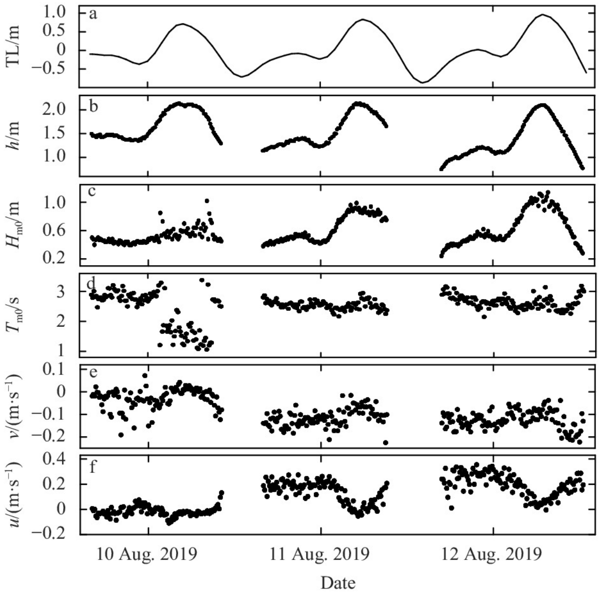

**Fig. 6.** Hydrodynamic conditions during the observation period of tide level (TL) (a), water depth ($h$) (b), mean wave height ($H_{m0}$) (c), mean wave period ($T_{m0}$) (d), mean cross-shore current velocity ($v$) (e), and mean alongshore current velocity ($u$) (f).

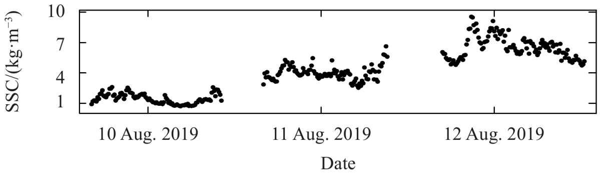

**Fig. 7.** SSC variation during the observation period.

results are presented in Fig. 8. The extreme SSC event fractions (hereafter referred to as $n_1/n$(SSC)) and the SSC percentage contained in the extreme events (hereafter referred to as $n_1m_1/nm$(SSC)) had minimum values of 0%, which mainly occurred between Bursts 1–109 and 176–211, and the maximum values of 100% which occurred six times after Burst 211. Moreover, as shown in Fig. 8, the extreme SSC events occurred more frequently between Bursts 235–318, with mean $n_1/n$(SSC) and $n_1m_1/nm$(SSC) values of 40.81% and 45.27%, respectively, which were significantly larger than those of the total bursts (10.88% and 12.57% for $n_1/n$(SSC) and $n_1m_1/nm$(SSC), respectively, shown in Table 2). This period could be divided by Burst 264. The mean $n_1/n$(SSC) and $n_1m_1/nm$(SSC) values of Bursts 235–264 were 67.81% and 69.74%, respectively, which were larger than those of Bursts 265–318 (25.82% and 31.68% for $n_1/n$(SSC) and $n_1m_1/nm$(SSC), respectively), indicating the extreme SSC events occurred most frequently between Bursts 235–264.

### 4.3 *Influence of TKE on SSC*

As shown in Fig. 9, the mean TKE values ranged from 0.14–33.98 kg/(m·s$^2$). The TKE was significantly lower during Period D1 (Bursts 1–109), with a mean value of 0.36 kg/(m·s$^2$), compared to the other periods. The TKE variation was small during Period D2 (Bursts 110–231); however, the mean TKE value increased to 2.37 kg/(m·s$^2$), which was remarkably higher than that of Period D1. During Period D3 (Bursts 232–332), the TKE was significantly higher than those of the other periods, with a mean value of 6.02 kg/(m·s$^2$), and the maximum TKE occurred between Bursts 239–278 with a mean value of 9.63 kg/(m·s$^2$).

The extreme TKE events were also analyzed, and the results are presented in Fig. 10. The fractions of extreme TKE events (hereafter referred to as $n_1/n$(TKE)) ranged from 0%–80.67%, and the TKE percentage contained in the extreme events (hereafter referred to as $n_1m_1/nm$(TKE)) ranged from 0%–99.09%. The minimum $n_1/n$(TKE) and $n_1m_1/nm$(TKE) values mainly occurred between Bursts 54–98, while the maximum values occurred in Burst 243. Based on the calculated $n_1/n$(TKE) results, the extreme TKE events occurred more frequently between Bursts 110–332 and 239–278, which had mean $n_1/n$(TKE) values of 21.75% and 42.65%, respectively, with the latter value being 14.79% greater than that of the total bursts. As shown in Table 2, the TKE had a smaller standard deviation of $n_1/n$ than the SSC, indicating the distribution of extreme TKE events during the observation period was less concentrated than the distribution of extreme SSC events. Therefore, it can be concluded that the TKE had a longer high incidence period of extreme events than the SSC (Bursts 235–318) during the observation period. Moreover, based on the $n_1m_1/nm$(TKE) calculation results, $n_1m_1/nm$(TKE) was significantly larger than $n_1/n$(TKE) during extreme TKE events, indicating that during extreme events, TKE differed from that in normal events. Furthermore, extreme events had a greater effect on TKE than SSC.

Generally, the SSC and TKE variation trends were similar; however, the TKE variation range was significantly larger than that of the SSC. As shown in Figs 9 and 10, the extreme TKE events occurred most frequently, and the TKE was significantly higher among Bursts 239–278 than the other bursts; therefore, the extreme event influence was probably more significant on TKE than SSC. In the high incidence period of extreme events, the TKE increase was significantly larger than during the other

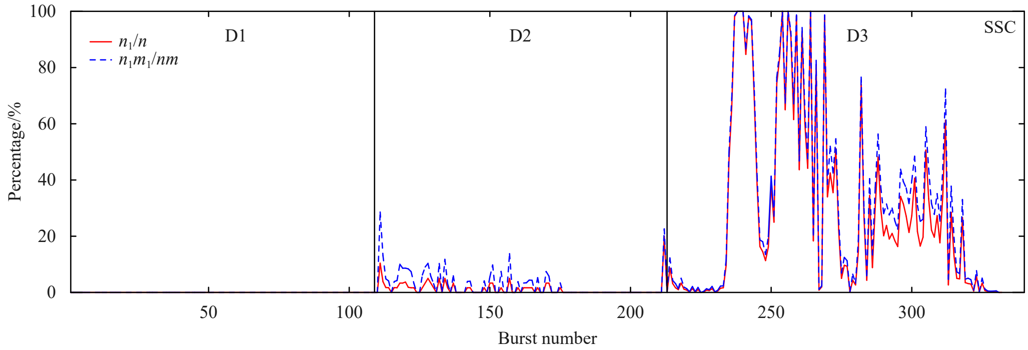

**Fig. 8.** Fractions of extreme SSC events to the total data points ($n_1/n$) and the SSC percentage contained in the extreme events in the entire time series ($n_1m_1/nm$).

**Table 2.** Statistical average of extreme events of overall bursts (332)

| Parameter | $(n_1/n)$/% | $(n_0/n_1)$/% | $(n_1m_1/nm)$/% | $(n_0m_0/nm)$/% |
|---|---|---|---|---|
| SSC | 10.88 (23.64) | 11.31 (20.06) | 12.57 (24.62) | 4.02 (10.73) |
| TKE | 14.79 (14.90) | 10.93 (24.17) | 41.80 (32.69) | 8.81 (20.58) |

Note: Data are shown as the mean value (standard deviation).

periods.

Utilizing the high-resolution TKE and SSC data, an extreme event analysis was performed to investigate their relationship. As shown in Fig. 11a, the fraction of correlated extreme events to extreme SSC events (hereafter referred to as $n_0/n_1$(SSC)) had minimum values of 0%, which mainly occurred in the same periods as the $n_1/n$(SSC) (Bursts 1–109 and 176–211), and maximum values of 100% which occurred at Bursts 114, 116, 230, and 278. From Bursts 239–280, the correlated extreme events occurred more frequently, and the $n_0/n_1$(SSC) values, with a mean value of 45.00%, were significantly larger than those of the other bursts. Furthermore, the SSC percentage contained in the correlated extreme events (hereafter referred to as $n_0m_0/nm$(SSC)) had minimum values of 0%, which mainly occurred in the same periods as the $n_1/n$(SSC), and the maximum value of 78.30% occurred at Burst 243. The $n_0m_0/nm$(SSC) values among Bursts 235–264, with a mean value of 29.00%, were larger than those of the other bursts and occurred during the same high incidence period as the extreme SSC events.

As shown in Fig. 11b, the fraction of correlated extreme events to TKE extreme events (hereafter referred to as $n_0/n_1$(TKE)) had minimum values of 0%, which mainly occurred between Bursts 1–211, and maximum values of 100% which occurred 6 times after Burst 211. The TKE percentage contained in the correlated extreme events (hereafter referred to as $n_0m_0/nm$(TKE)) had minimum values of 0%, which mainly occurred in the same period as the minimum $n_0/n_1$(TKE), and the maximum value of 78.30% occurred at Burst 240. Based on the SSC extreme event calculation results, extreme SSC events rarely occurred from Bursts 1–211, causing an $n_0$ value of zero for most bursts. However, from Bursts 235–318, the extreme SSC and TKE events occurred more frequently, and the number of extreme SSC events was significantly higher than that of TKE, which increased the $n_0/n_1$(TKE) value. As shown in Table 3, the mean $n_0/n_1$(TKE) and $n_0m_0/nm$(TKE) values from Bursts 235–318 were 41.60% and 34.25%, respectively, and both were greater than those of all the other bursts. Therefore, it can be concluded that the extreme SSC event distribution was more concentrated than the extreme TKE event distribution during the observation period.

As shown in Table 3, from Bursts 235–318, the mean $n_0/n_1$(SSC) value was 30.72%, and the mean $n_0m_0/nm$(SSC) value was smaller than the mean $n_1m_1/nm$(SSC) value, indicating that approximately 15% of the sediment suspension motion was associated with turbulent motion, and other factors could influence sediment motion. Furthermore, the mean $n_0/n_1$(TKE) value was 41.60%, and the mean $n_0m_0/nm$(TKE) value was smaller than the mean $n_1m_1/nm$(TKE) value, indicating that in the high incidence period of extreme events, approximately 34% of the turbulent motion contributed to sediment suspension, and portions of the

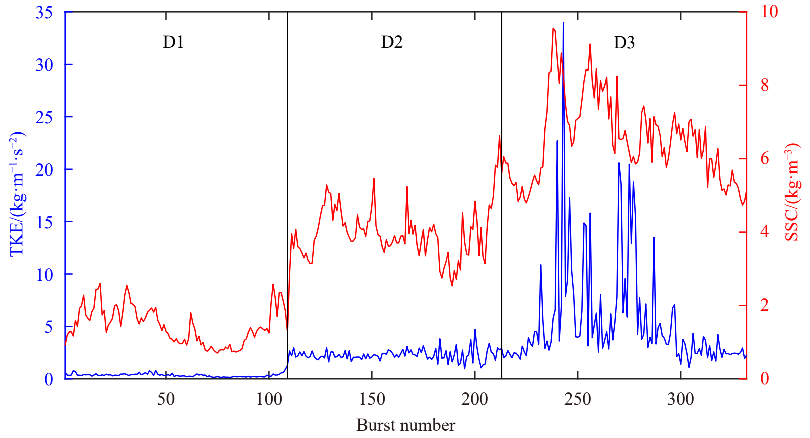

**Fig. 9.** Mean TKE and SSC values for each burst.

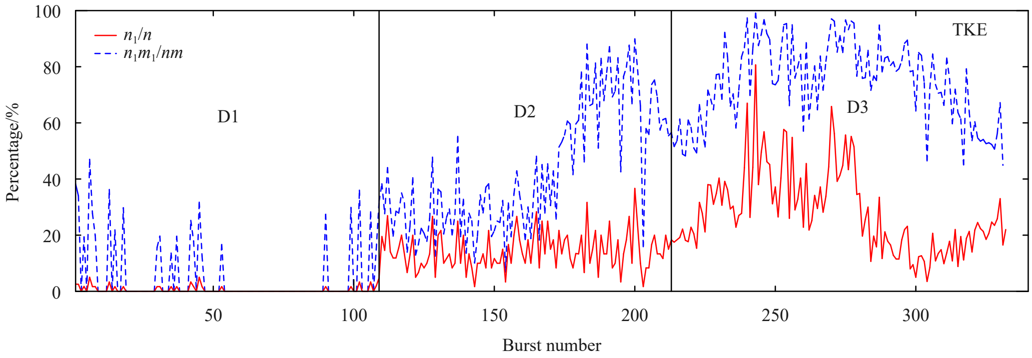

**Fig. 10.** Fractions of extreme TKE events to the total data points ($n_1/n$) and the TKE percentage contained in the extreme events in the entire data set ($n_1m_1/nm$).

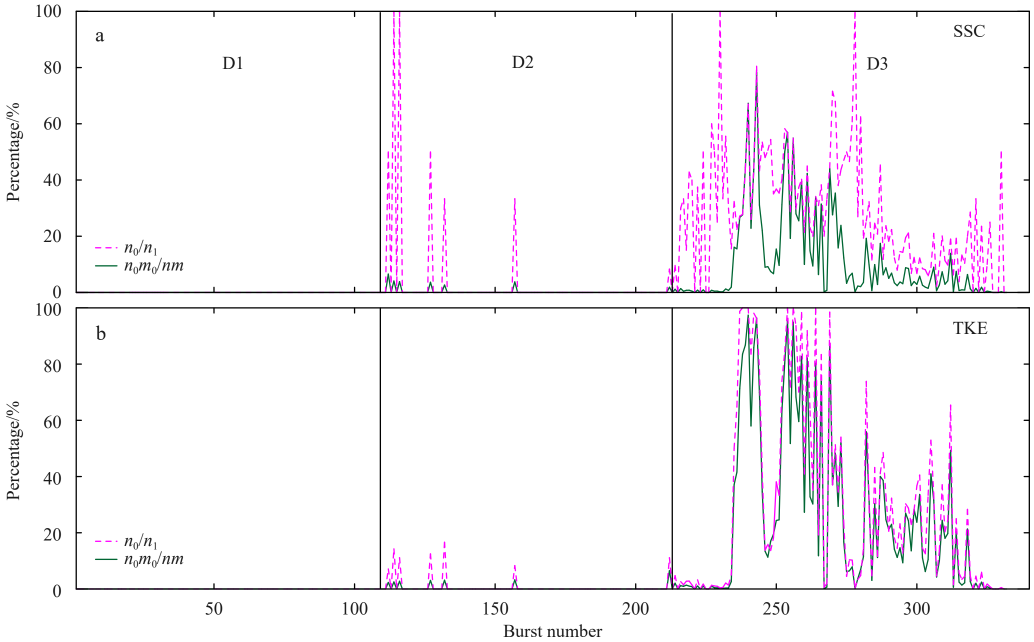

**Fig. 11.** The fractions of correlated extreme events to the SSC (a) / TKE (b) extreme events ($n_0/n_1$) and the percent of the SSC (a) / TKE (b) contained in the correlated extreme events in relation to that in the entire time series ($n_0m_0/nm$).

**Table 3.** Statistical averages of extreme events from Bursts 235–318

| Parameter | $(n_1/n)$/% | $(n_0/n_1)$/% | $(n_1m_1/nm)$/% | $(n_0m_0/nm)$/% | $(n_0/n)$/% |
|---|---|---|---|---|---|
| SSC | 40.82 | 30.72 | 45.27 | 15.36 | 14.35 |
| | (31.57) | (19.52) | (30.44) | (16.76) | (16.78) |
| TKE | 29.37 | 41.60 | 79.77 | 34.25 | 14.35 |
| | (16.62) | (32.18) | (11.60) | (28.39) | (16.78) |

Note: Data are shown as the mean value (standard deviation).

TKE dissipated directly into the water column. Generally, the fraction of correlated extreme events to the total data points ($n_0/n$) was 14.35%, indicating that in addition to TKE, other factors affect the SSC variation.

### 4.4 *Influence of BSS on SSC*

The mean SSC values and the corresponding wave-induced BSS ($\tau_w$), current-induced BSS ($\tau_c$), and combined wave-current BSS ($\tau_{cw}$) of each burst were calculated to evaluate the relationship between SSC and BSS. The results showed that $\tau_w$ and $\tau_c$ ranged from 0.002–3.060 Pa (mean value=1.50 Pa) and 0.001–0.900 Pa (mean value=0.31 Pa), respectively, showing $\tau_w$ was an order of magnitude larger than $\tau_c$. Additionally, $\tau_{cw}$ ranged from 0.002–3.60 Pa (mean value=1.80 Pa) and the critical BSS ($\tau_{cr}$) was 0.16 Pa. As shown in Fig. 12, from Bursts 67–101, $\tau_{cw}$ was smaller than $\tau_{cr}$ for some bursts, which corresponds with the low SSC value period; however, the majority of the time, $\tau_{cw}$ was an order of magnitude larger than $\tau_{cr}$, which indicates the WCI was strong enough to drive sediment incipience and resuspension.

As shown in Table 4, based on the extreme event analysis results, $\tau_{cw}$ had the greatest correlated extreme events with an $n_0/n$ of 20.86%, while the $n_0/n$ of $\tau_c$ was significantly less than those of $\tau_{cw}$ and $\tau_w$. Moreover, based on the $n_0m_0/nm$(SSC) values, during extreme event periods, in which the maximum $n_0m_0/nm$(SSC) occurred, approximately 36% and 30% of the sediment suspen-

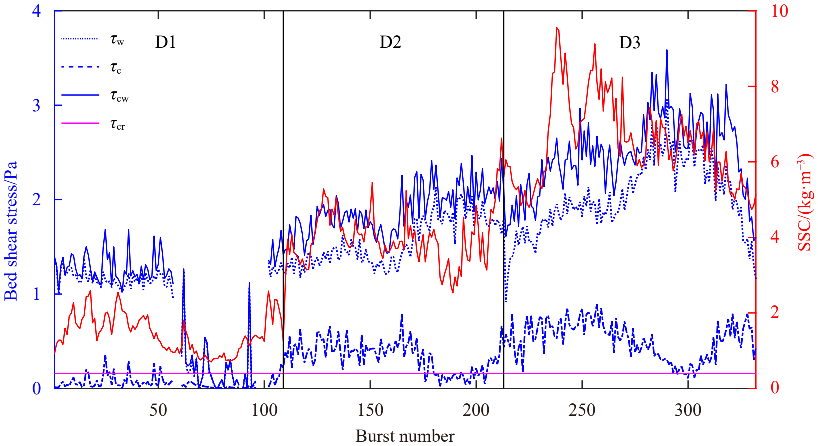

**Fig. 12.** Wave-induced BSS ($\tau_w$), current-induced BSS ($\tau_c$), combined wave-current BSS ($\tau_{cw}$), and mean SSC value of each burst. The horizontal magenta line indicates the critical BSS ($\tau_{cr}$=0.16 Pa).

**Table 4.** Extreme event analysis results utilizing the comparison parameters of wave-induced BBS ($\tau_{\rm w}$), current-induced BBS ($\tau_{\rm c}$), and combined wave-current BSS ($\tau_{\rm cw}$)

| Parameter | $(n_0/n)$/% | $(n_0m_0/nm(\text{SSC}))$/% |
|---|---|---|
| $\tau_{\rm w}$ | 18.71 | 31.35 |
| $\tau_{\rm c}$ | 13.80 | 25.04 |
| $\tau_{\rm cw}$ | 20.86 | 35.61 |

Notes: $n_0$ is the number of correlated extreme events where the extreme SSC events and comparison parameters occur synchronously, $n$ is the number of total data points (332), $m_0$ is the mean SSC value of the correlated extreme event data points, and $m$ is the mean SSC value of the total data points.

sion motion were correlated with $\tau_{\rm cw}$ and $\tau_{\rm w}$, respectively. The $\tau_{\rm c}$ variation had less influence on the SSC than the $\tau_{\rm w}$ influence because $\tau_{\rm c}$ was an order of magnitude smaller than $\tau_{\rm w}$ (Fig. 12), and the $n_0m_0/nm$ of $\tau_{\rm c}$ was 25.04%. Based on these results, the $\tau_{\rm cw}$ and $\tau_{\rm w}$ influences were much greater than that of $\tau_{\rm c}$ on the SSC variation.

Based on the linear regression results between SSC and BSS (Fig. 13), $\tau_{\rm cw}$ had the best fitting effect with an $R^2$ value of 0.70, while the $R^2$ values of $\tau_{\rm w}$ and $\tau_{\rm c}$ were similar. These results demonstrate a statistically significant relationship between SSC and BSS, and SSC is best correlated with $\tau_{\rm cw}$.

The data quality of each group satisfied the $r_{\rm p}$ and $r_{\rm s}$ calculation requirements. As shown in Table 5, there was a good correlation between SSC and BSS, and the $r_{\rm p}$ and $r_{\rm s}$ values were both approximately 0.8, and $\tau_{\rm cw}$ had the highest correlation with $r_{\rm p}$ and $r_{\rm s}$ values of 0.84 and 0.89, respectively.

The variation of SSCs and BSS during the observation were shown in Fig. 12. As mentioned above, $\tau_{\rm c}$ was smaller than $\tau_{\rm w}$, which indicates that the $\tau_{\rm cw}$ variation was mainly affected by $\tau_{\rm w}$. Generally, $\tau_{\rm cw}$ and $\tau_{\rm w}$ had similar variation trends, with both significantly increasing during the observation period. The $\tau_{\rm cw}$ and $\tau_{\rm w}$ values were significantly larger from Bursts 101–332 than from Bursts 1–100, similar to the SSC variation trend. Based on these findings, it can be concluded that $\tau_{\rm cw}$ has a significant effect on sediment mobilization and the resulting suspended sediment entrainment.

## 5 Discussion

Previous studies have demonstrated that wave conditions significantly influence suspended sediment variation and that wave type and the distance from the breakpoint may govern SSC in the surf zone (Beach and Sternberg, 1996). The dominant wave conditions are determined by relative wave height ($H_{\rm r}$), which can be calculated as follows:

$$H_{\rm r}=\frac{H_{\rm m0}}{h}. \tag{25}$$

Some studies have shown that breaking waves are the sediment-suspending mechanism, which is consistent with previous studies that have determined that SSC and TKE are significantly larger under breaking wave ($0.3<H_{\rm r}<0.6$) and surf bore conditions ($H_{\rm r}>0.6$) than under non-breaking wave conditions ($H_{\rm r}<0.3$) (Conley and Beach, 2003; Hansen and Svendsen, 1984). During the observation period of this study, the instrument site was under breaking wave conditions most of the time (Fig. 14); therefore, the wave conditions should significantly influence SSC, and the wave effect can be evaluated utilizing $h$ and $H_{\rm m0}$.

The extreme event analysis method was used to evaluate the relationship among SSCs and water depth, mean wave height, relative wave height. As shown in Table 6, the relative wave height had most correlated extreme events with $n_0/n$ reaching 18.10%, which was close to the $n_0/n$ of combined wave-current BSS and wave-induced BBS (20.86% and 18.71%, respectively), while the $n_0/n$ of water depth and mean wave height were apparently smaller. Furthermore, based on the calculation results of $n_0m_0/nm$ (SSC), during extreme events period, approximately 30% of sediment suspension motion was correlated with relative wave height, which was also close to the $n_0m_0/nm(\text{SSC})$ of combined wave-current BSS and wave-induced BBS (35.61% and 31.35%, respectively). Therefore, it could be considered that compared with combined wave-current BSS and wave-induced BBS, relative wave height had the similar influence degree on SSC variation.

Based on the linear regression results (Fig. 15), $h$ and $H_{\rm m0}$ were poorly correlated with SSC ($R^2$=0.15 and 0.06, respectively); however, $H_{\rm r}$ was highly correlated with SSC with an $R^2$ value of 0.62, which was similar to those of $\tau_{\rm cw}$ and $\tau_{\rm w}$ ($R^2$=0.61 and 0.70, respectively, Fig. 13) and higher than the $h$ and $H_{\rm m0}$ $R^2$ values.

The $r_{\rm p}$ and $r_{\rm s}$ calculation results were consistent with the linear regression results. As shown in Table 7, $H_{\rm r}$ had a higher correlation degree with SSC ($r_{\rm p}$=0.82, $r_{\rm s}$=0.84) than with $h$ or $H_{\rm m0}$, and was similar to those of $\tau_{\rm cw}$ and $\tau_{\rm w}$.

The SSC and $H_{\rm r}$ variations during the observation period are presented in Fig. 14. Generally, $H_{\rm r}$ significantly increased during the observation period. Except for a few early period bursts that were significantly higher, the $H_{\rm r}$ of Bursts 1–100 was smaller than that of Bursts 101–332, similar to the SSC variation trend.

If $h$ and $H_{\rm m0}$ are analyzed separately, they have little influence on SSC; however, if the relative importance of $h$ and $H_{\rm m0}$ is considered by calculating $H_{\rm r}$, and $H_{\rm r}$ is determined to impact SSC variation significantly and has a similar correlation degree with

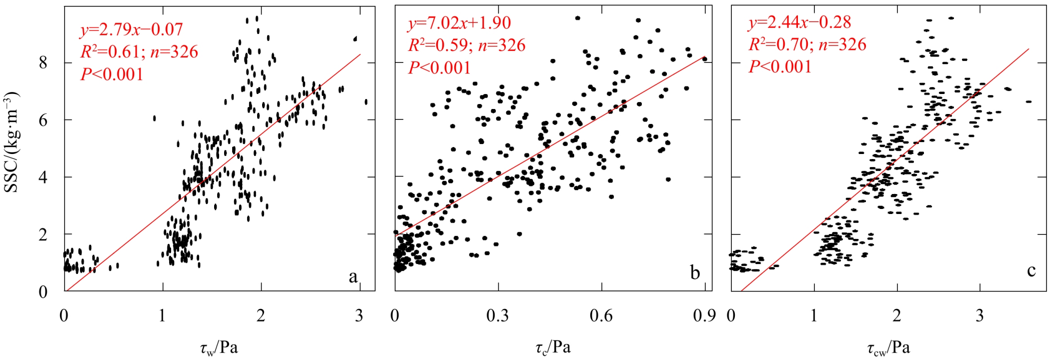

**Fig. 13.** Linear regression results between SSC and wave-induced BSS (a), current-induced BSS (b), and combined wave-current BSS (c).

**Table 5.** Evaluation of the relationship between SSC and wave-induced BSS ($\tau_w$), current-induced BSS ($\tau_c$), and combined wave-current BSS ($\tau_{cw}$) via the Pearson ($r_p$) and Spearman rank ($r_s$) correlation coefficients

| Parameter | $r_p$ | $r_s$ |
|---|---|---|
| $\tau_w$ | 0.78 | 0.84 |
| $\tau_c$ | 0.77 | 0.79 |
| $\tau_{cw}$ | 0.84 | 0.89 |

those of $\tau_{cw}$ and $\tau_w$. According to a previous study (Van Rijn, 2007), in coastal zones with small velocities (0.1–0.6 m/s), suspended sediment transport can be strongly dependent on $H_r$; therefore, the combined effects of *h* and wave height can have significant influence on SSC variation. When analyzing the SSC influence factors, the effects of *h* and wave height should be considered conjunctively, which can affect SSC variation in the ways different from TKE and BSS.

Generally, wave height variations are the major cause of variations in the mean SSC in the water column and influence the sediment entrainment due to their significant contribution to the sediment suspension mechanism compared to other factors, such as bed configuration and mean current (Aagaard and Greenwood, 1995; Liang et al., 2007; Pang et al., 2020). Both waves and tidal current can lead to sediment resuspension (Fan et al., 2019). During the observation period, as the tidal range increased, the impact of the tide was enhanced, and the lowest tide level decreased gradually, resulting in a reduced minimum *h* from Period D1 to D3 (Fig. 6a). During the ebb tide period among Bursts 214–269, *h* was smaller than in the other periods, while SSC increased significantly and the maximum SSC value occurred. The measure results indicate that strong tide effect may enhance the local resuspension and cause high SSC.

In addition, it has been determined that tidal flow plays an important role in horizontal advection which is the main contributor to sediment transport and high SSCs (Xiong et al., 2017; Yang et al., 2016; Yu et al., 2012). In the radial sand ridge system of the southern Yellow Sea, the model simulation suggested that the distribution of SSC was strongly affected by the tidal current (Xing et al., 2012). Moreover, under insignificant wave conditions, the tidal reciprocating flow can affect the sediment resuspension process and cause SSC flood-ebb asymmetry, resulting

**Table 6.** Extreme event analysis results utilizing the comparison parameters of water depth (*h*), mean wave height ($H_{m0}$), and relative wave height ($H_r$)

| Parameter | $(n_0/n)$/% | $(n_0m_0/nm(\text{SSC}))$/% |
|---|---|---|
| *h* | 5.83 | 9.44 |
| $H_{m0}$ | 11.66 | 18.63 |
| $H_r$ | 18.10 | 30.30 |

Notes: $n_0$ is the number of correlated extreme events where the extreme SSC events and comparison parameters occur synchronously, *n* is the number of total data points (332), $m_0$ is the mean SSC of the correlated extreme event data points, and *m* is the mean SSC of the total data points.

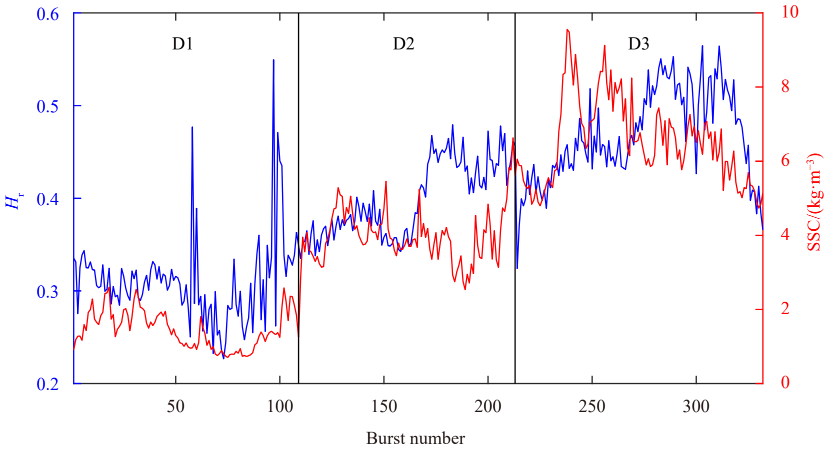

**Fig. 14.** Relative wave height ($H_r$) and SSC of all the bursts.

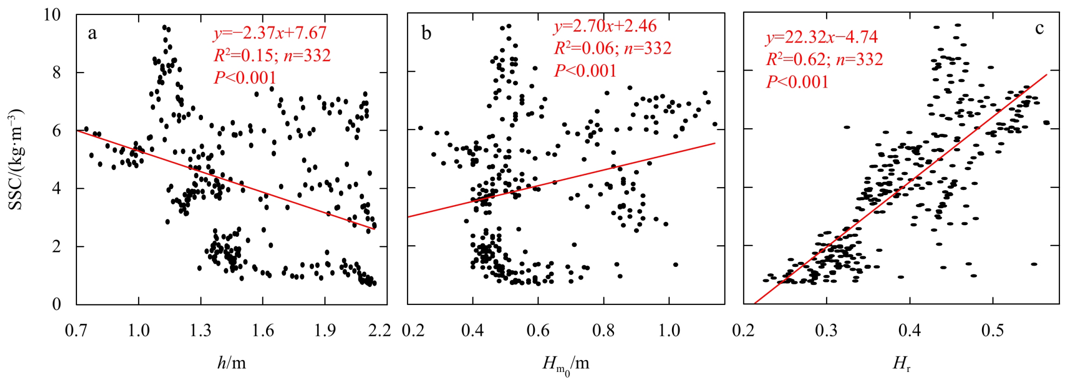

**Fig. 15.** Linear regression results between SSC and water depth (*h*) (a), mean wave height ($H_{m0}$) (b), and relative wave height ($H_r$) (c).

**Table 7.** Evaluation of the relationship between SSC and water depth ($h$), mean wave height ($H_{m0}$), relative wave height ($H_r$) via the Pearson correlation coefficient ($r_p$) and Spearman rank correlation coefficients ($r_s$)

| Parameter | $r_p$ | $r_s$ |
|---|---|---|
| $h$ | −0.37 | −0.44 |
| $H_{m0}$ | 0.27 | 0.25 |
| $H_r$ | 0.82 | 0.84 |

in SSC variation (Fan et al., 2019). Therefore, further studies are necessary to comprehensively explore the way how tide influences SSC on the beaches.

## 6 Conclusions

The findings from this study are summarized below:

(1) TKE is higher during extreme event periods than during normal events, and extreme events have a greater effect on TKE than on SSC.

(2) TKE is one of the critical factors affecting SSC variation. Based on the field observation data, approximately 15% of the sediment suspension motion was associated with turbulent motion during the high incidence period of extreme events, approximately 34% of the turbulent motion contributed to sediment suspension, and a portion of the TKE dissipated directly into the water column. The correlated extreme events accounted for 14.35% of the total observation period.

(3) During the observation period, the WCI was strong enough to drive sediment incipience and resuspension most of the time, and $\tau_{cw}$ and $\tau_w$ have a greater influence on suspended sediment transport and SSC variation compared with that of $\tau_c$. During extreme event periods, approximately 36% and 30% of the sediment suspension motion were attributed to $\tau_{cw}$ and $\tau_w$, respectively.

(4) $H_r$ is highly correlated with SSC, indicating that the combined effects of $h$ and wave height can significantly affect SSC variation. In the nearshore regions, $h$ is mainly controlled by the tide; therefore, when analyzing the factors influencing SSC, the effects of tides and waves should be considered conjunctively.

## References

Aagaard T, Greenwood B. 1995. Suspended sediment transport and morphological response on a dissipative beach. Continental Shelf Research, 15(9): 1061–1086, doi: 10.1016/0278-4343(94)00068-X

Aagaard T, Greenwood B, Hughes M. 2013. Sediment transport on dissipative, intermediate and reflective beaches. Earth-Science Reviews, 124: 32–50, doi: 10.1016/j.earscirev.2013.05.002

Aagaard T, Hughes M G. 2006. Sediment suspension and turbulence in the swash zone of dissipative beaches. Marine Geology, 228(1–2): 117–135

Aagaard T, Hughes M G. 2010. Breaker turbulence and sediment suspension in the surf zone. Marine Geology, 271(3–4): 250–259, doi: 10.1016/j.margeo.2010.02.019

Beach R A, Sternberg R W. 1996. Suspended-sediment transport in the surf zone: response to breaking waves. Continental Shelf Research, 16(15): 1989–2003, doi: 10.1016/0278-4343(96)00029-5

Bolaños R, Thorne P D, Wolf J. 2012. Comparison of measurements and models of bed stress, bedforms and suspended sediments under combined currents and waves. Coastal Engineering, 62: 19–30, doi: 10.1016/j.coastaleng.2011.12.005

Brenninkmeyer S J B. 1976. *In situ* measurements of rapidly fluctuating, high sediment concentrations. Marine Geology, 20(2): 117–128, doi: 10.1016/0025-3227(76)90082-7

Conley D C, Beach R A. 2003. Cross-shore sediment transport partitioning in the nearshore during a storm event. Journal of Geophysical Research: Oceans, 108(C3): 3065, doi: 10.1029/2001JC001230

Cox D T, Anderson S L. 2001. Statistics of intermittent surf zone turbulence and observations of large eddies using PIV. Coastal Engineering Journal, 43(2): 121–131, doi: 10.1142/S057856340100030X

Cox D T, Kobayashi N. 2000. Identification of intense, intermittent coherent motions under shoaling and breaking waves. Journal of Geophysical Research: Oceans, 105(C6): 14223–14236, doi: 10.1029/2000JC900048

Fan Renfu, Wei Hao, Zhao Liang, et al. 2019. Identify the impacts of waves and tides to coastal suspended sediment concentration based on high-frequency acoustic observations. Marine Geology, 408: 154–164, doi: 10.1016/j.margeo.2018.12.005

Folk R L, Ward W C. 1957. Brazos River bar [Texas]; a study in the significance of grain size parameters. Journal of Sedimentary Research, 27(1): 3–26, doi: 10.1306/74D70646-2B21-11D7-8648000102C1865D

Foster D L, Beach R A, Holman R A. 2000. Field observations of the wave bottom boundary layer. Journal of Geophysical Research: Oceans, 105(C8): 19631–19647, doi: 10.1029/1999JC900018

Foster D L, Beach R A, Holman R A. 2006. Turbulence observations of the nearshore wave bottom boundary layer. Journal of Geophysical Research: Oceans, 111(C4): C04011

Grant W D, Madsen O S. 1979. Combined wave and current interaction with a rough bottom. Journal of Geophysical Research: Oceans, 84(C4): 1797–1808, doi: 10.1029/JC084iC04p01797

Hansen J B, Svendsen I A. 1984. A theoretical and experimental study of undertow. In: Conference of 19th International Conference on Coastal Engineering. Houston: ASCE, 2246–2262

Jaffe B, Sallenger A Jr. 1992. The contribution of suspension events to sediment transport in the surf zone. In: Conference of 23rd International Conference on Coastal Engineering. Venice: ASCE, 2680–2693

Jia Liangwen, Ren Jie, Nie Dan, et al. 2014. Wave-current bottom shear stresses and sediment re-suspension in the mouth bar of the Modaomen Estuary during the dry season. Acta Oceanologica Sinica, 33(7): 107–115, doi: 10.1007/s13131-014-0510-x

Jing L, Ridd P V. 1996. Wave-current bottom shear stresses and sediment resuspension in Cleveland Bay, Australia. Coastal Engineering, 29(1–2): 169–186, doi: 10.1016/S0378-3839(96)00023-3

Jonsson I G. 1966. Wave boundary layers and friction factors. In: Conference of 10th International Conference on Coastal Engineering. Tokyo: ASCE, 127–148

Kos'yan R D, Kunz H, Kuznetsov S Y, et al. 1996. Sand suspension events and intermittence of turbulence in the surf zone. In: Conference of 25th International Conference on Coastal Engineering. Orlando: ASCE, 4111–4119

LeClaire P D, Ting F C K. 2017. Measurements of suspended sediment transport and turbulent coherent structures induced by breaking waves using two-phase volumetric three-component velocimetry. Coastal Engineering, 121: 56–76, doi: 10.1016/j.coastaleng.2016.11.008

Liang Bingchen, Li Huajun, Lee D. 2007. Numerical study of three-dimensional suspended sediment transport in waves and currents. Ocean Engineering, 34(11–12): 1569–1583, doi: 10.1016/j.oceaneng.2006.12.002

Maity S K, Maiti R. 2016. Analysis of sedimentation in connection to grain size and shear stress at lower reach of the Rupnarayan River, West Bengal, India. Indian Journal of Geo-Marine Sciences, 45(9): 1128–1137

Nahler G. 2009. Pearson correlation coefficient. In: Nahler G, ed. Dictionary of Pharmaceutical Medicine. Vienna: Springer Vienna, 132

Nielsen P. 1992. Coastal Bottom Boundary Layers and Sediment Transport. Singapore: World Scientific

Ogston A S, Sternberg R W. 1995. On the importance of nearbed sediment flux measurements for estimating sediment transport in the surf zone. Continental Shelf Research, 15(13): 1515–1524, doi: 10.1016/0278-4343(95)00036-Z

Pang Wenhong, Dai Zhijun, Ge Zhenpeng, et al. 2019. Near-bed cross-shore suspended sediment transport over a meso-macro tidal beach under varied wave conditions. Estuarine, Coastal and Shelf Science, 217: 69–80

Pang Wenhong, Dai Zhijun, Ma Binbin, et al. 2020. Linkage between turbulent kinetic energy, waves and suspended sediment concentrations in the nearshore zone. Marine Geology, 425: 106190, doi: 10.1016/j.margeo.2020.106190

Ruessink B G. 2010. Observations of turbulence within a natural surf zone. Journal of Physical Oceanography, 40(12): 2696–2712, doi: 10.1175/2010JPO4466.1

Signell R P, Beardsley R C, Graber H C, et al. 1990. Effect of wave-current interaction on wind-driven circulation in narrow, shallow embayments. Journal of Geophysical Research: Oceans, 95(C6): 9671–9678, doi: 10.1029/JC095iC06p09671

Smyth C, Hay A E. 2003. Near-bed turbulence and bottom friction during SandyDuck97. Journal of Geophysical Research: Oceans, 108(C6): 3197, doi: 10.1029/2001JC000952

Soulsby R L. 1997. The Dynamics of Marine Sands: A Manual for Practical Applications. London: Thomas Thelford

Soulsby R L, Hamm L, Klopman G, et al. 1993. Wave-current interaction within and outside the bottom boundary layer. Coastal Engineering, 21(1–3): 41–69, doi: 10.1016/0378-3839(93)90045-A

Spearman C. 1904. The proof and measurement of association between two things. The American Journal of Psychology, 15(1): 72–101, doi: 10.2307/1412159

Swart D H. 1974. Offshore sediment transport and equilibrium beach profiles [dissertation]. Delft, Netherlands: Delft Hydraulics Laboratory

Van Rijn L C. 2007. Unified view of sediment transport by currents and waves. II: suspended transport. Journal of Hydraulic Engineering, 133(6): 668–689, doi: 10.1061/(ASCE)0733-9429(2007)133:6(668)

Xing Fei, Wang Yaping, Wang H V. 2012. Tidal hydrodynamics and fine-grained sediment transport on the radial sand ridge system in the southern Yellow Sea. Marine Geology, 291–294: 192–210

Xiong Jilian, Wang Xiaohua, Wang Yaping, et al. 2017. Mechanisms of maintaining high suspended sediment concentration over tide-dominated offshore shoals in the southern Yellow Sea. Estuarine, Coastal and Shelf Science, 191: 221–233

Yang Yang, Wang Yaping, Gao Shu, et al. 2016. Sediment resuspension in tidally dominated coastal environments: new insights into the threshold for initial movement. Ocean Dynamics, 66(3): 401–417, doi: 10.1007/s10236-016-0930-6

Yoon H D, Cox D T. 2012. Cross-shore variation of intermittent sediment suspension and turbulence induced by depth-limited wave breaking. Continental Shelf Research, 47: 93–106, doi: 10.1016/j.csr.2012.07.001

Yu Qian, Wang Yaping, Flemming B, et al. 2012. Tide-induced suspended sediment transport: depth-averaged concentrations and horizontal residual fluxes. Continental Shelf Research, 34: 53–63, doi: 10.1016/j.csr.2011.11.015

Zar J H. 1972. Significance testing of the Spearman rank correlation coefficient. Journal of the American Statistical Association, 67(339): 578–580, doi: 10.1080/01621459.1972.10481251